Reconstruction of the vibronic-state density matrix based on pump-probe state-resolved energy spectra

Shan Xue, Shaohua Sun, Pengji Ding, Bitao Hu, Shengjun Yue,* and Hongchuan Du†
School of Nuclear Science and Technology, Lanzhou University, Lanzhou 730000, China
and Key Laboratory of Special Function Materials and Structure Design, Ministry of Education, Lanzhou University, Lanzhou 730000, China

(Received 3 November 2021; revised 18 March 2022; accepted 28 March 2022; published 8 April 2022)

We propose a scheme based on perturbation theory to reconstruct a molecular density matrix (DM) using the pump-probe state-resolved energy spectra. By applying the scheme to an O_2^+ system produced via strong-field ionization, we demonstrate that the reconstruction scheme can retrieve the populations and coherences of vibrational-electronic (vibronic) states while maintaining good robustness. We further extend the strong-field transient ionization model to include the rotational degree of freedom. The evolution of the vibronic-state DM can be recovered, benefiting from the population stabilities between adjacent fractional revivals. The retrieved signals quantitatively capture the distinguishing decay features of the vibronic coherences. Our strategy paves the way toward understanding elaborate vibronic-state DMs in molecular systems.

DOI: 10.1103/PhysRevA.105.043108

I. INTRODUCTION

Ultrafast coherent dynamics occurs after a set of ionic states are prepared coherently by laser ionization [1–4]. The established electronic coherences result in (sub)femtosecond electronic dynamics, which is often known as charge migration [4–7]. In molecular systems, the vibrational-electronic (vibronic) coherences correlate electronic dynamics with significantly slower nuclear motions. Such a process is referred to as charge transfer, which plays a key role in chemical reactions and biological processes [8,9]. Essentially, all information on "postionization" molecular dynamics is encoded in the reduced density matrix (DM) of ions, that is, ρ_{mn}, including the populations ρ_{mm} and coherences ρ_{mn} ($m \neq n$). To understand photoionization processes and manipulate the subsequent coherent dynamics, it is necessary to obtain the reduced DM of the ion ensemble.

In the last decade, different theoretical approaches were developed to simulate photoionization processes in atomic systems, such as the time-dependent configuration interaction singles (TDCIS) method [10–12], multiconfigurational time-dependent Hartree-Fock (MCTDHF) method [13], and time-dependent density functional theory (TDDFT) [14]. Using these methods, properties of the reduced DM were extensively studied, especially for ionic coherence [10,11,15,16]. In general, establishing coherence requires the bandwidth of the laser pulse to be greater than the energy separation between ionic states. Moreover, periodic ionization provided by multicycle strong-field infrared (IR) pulses or attosecond pulse trains can also selectively create ionic coherences [16,17]. In contrast, for molecules, calculating the reduced DM via full *ab initio* methods while considering both the nuclear motion and photoionization has been challenging to data. Instead, the sudden ionization assumption is often used to investigate the evolution of the DM in closed ionic systems. In this simplified model, the ionic vibronic states are fully coherent and the populations obey Franck-Condon (FC) distributions. Subsequently, the electronic coherences typically decay in a few femtoseconds owing to the interplay of multiple vibrational modes for polyatomic molecules [18–20]. Because of the theoretical difficulties in calculating the molecular reduced DM, it is important to obtain a method of reconstructing it from experimental detection signals.

With prior knowledge of the basis sets, complete determination of the DM elements leads to a tomographic reconstruction of a quantum state. For pure-state systems, the populations and coherences are strictly associated and can be retrieved simultaneously from the interference signals [21,22]. However, in mixed-state systems, the populations and coherences are not necessarily related; therefore, their reconstructions are independent. Over the last few decades, various strategies were proposed to achieve tomographic reconstructions of mixed states, including (i) nonlinear wave-packet interferometry [23], (ii) reconstruction from dedicated designed multidimensional spectroscopy [24], and (iii) reconstruction from terahertz-assisted photoelectron spectroscopy [25]. The time-evolved DM of Kr^+ has been experimentally reconstructed within subfemtosecond temporal accuracy using attosecond transient absorption spectroscopy (ATAS) [1]. In general, previous studies on mixed states mainly focused on few-state atomic systems, and related research on molecular systems is rare because of the complexities induced by nuclear motion. Recently, the modification of electronic coherence via vibronic dynamics was observed in Br_2^+ using ATAS, which is a promising step toward exploiting vibronic-state coherence [26].

In this paper, we propose a scheme to reconstruct the mixed-state DM for atoms and diatomic molecules. The

---

[*] yuesj@lzu.edu.cn

[†] duhch@lzu.edu.cn

scheme is based on perturbation theory in combination with state-resolved energy and quantum beat (QB) spectra. By applying the scheme on an O_2^+ system, we discuss its feasibility and robustness. Furthermore, this reconstruction scheme is found to work well even when considering molecular rotation.

The remainder of the paper is organized as follows. In Sec. II, we describe the theoretical framework, starting with the quantum Liouville equations (QLEs) in Sec. II A, then the principle of the reconstruction scheme in Sec. II B. Our results and discussions are presented in Sec. III. In Sec. III A, the reconstruction method is first applied to the O_2^+ system without considering molecular rotation. In Sec. III B, the strong-field transient ionization model is extended to include the rotational degree of freedom (RDOF). The scheme is then executed on O_2^+ while considering the RDOF. Our conclusions are summarized in Sec. IV. Note that atomic units are used throughout the paper unless otherwise indicated.

II. THEORETICAL METHODS

The following theoretical methods are developed for atomic and diatomic molecular systems and the reconstruction scheme is specifically established for diatomic molecular systems.

A. Quantum Liouville equations

To describe the interaction between an ionic system and probe pulses, we propagate the ionic DM by solving the QLEs. The density operator for a mixed state is expressed as

$$\hat{\rho} = \sum_k |\Phi^{(k)}\rangle P_k \langle\Phi^{(k)}|, \tag{1}$$

where P_k represents the probability that the ionic system is in a pure state $\Phi^{(k)}$. In a given basis of states, the DM can be expressed as ρ_{mn} with $m(n)$ representing the $m(n)$th state. Time evolution of the DM in the driving of a laser field $\boldsymbol{\mathcal{E}}(t)$ is described by the QLEs

$$i\frac{\partial}{\partial t}\rho_{mn} = (E_m - E_n)\rho_{mn} - \boldsymbol{\mathcal{E}}(t)\cdot\sum_o(\mathbf{u}_{mo}\rho_{on} - \rho_{mo}\mathbf{u}_{on}), \tag{2}$$

where $\mathbf{u}_{mn}$ is the transition dipole matrix (TDM) element between the states m and n. E_m is the mth-state eigenenergy.

To investigate molecular systems without the nonadiabatic couplings, the Born-Oppenheimer (BO) approximation is usually used [27,28]. Specifically, in the following example of O_2^+, where there is no avoided crossing among the states $a^4\Pi_u$, $b^4\Sigma_g^-$, and $f^4\Pi_g$ [shown in Fig. 2(b)], the nonadiabatic coupling can be considered negligible, and the BO approximation is a good approximation. Molecular dynamics near an avoided crossing or conical intersection is usually complex and such nonadiabatic dynamics is beyond the scope of this work [29]. In the BO approximation, the DM can be expressed in terms of vibronic states $\rho_{ij}^{mn} = \langle\psi_m\chi_i^m|\hat{\rho}|\psi_n\chi_j^n\rangle$. Here, $\chi_i^m(R)$ and $\psi_m(\mathbf{r};R)$ are the wave functions of the ith vibrational state on the mth potential energy curve (PEC) and the mth electronic state, respectively. $\mathbf{r}$ and R refer to the electronic and nuclear coordinates, respectively. Then, the vibronic-state QLEs are expressed as

$$i\frac{\partial}{\partial t}\rho_{ij}^{mn} = \left(E_i^m - E_j^n\right)\rho_{ij}^{mn} - \boldsymbol{\mathcal{E}}(t)\cdot\sum_{o,l}\left(\mathbf{u}_{il}^{mo}\rho_{lj}^{on} - \rho_{il}^{mo}\mathbf{u}_{lj}^{on}\right), \tag{3}$$

where $\mathbf{u}_{ij}^{mn} = \langle\chi_i^m|\mathbf{u}_{mn}(R)|\chi_j^n\rangle$ is the vibronic-state TDM element. E_i^m is the eigenenergy of state $|\psi_m\chi_i^m\rangle$.

If the interaction occurs over a longer time, for example, on a several-picosecond timescale, the molecular rotation cannot be ignored. To include the RDOF, the density operator need to be expanded in the rotational-vibronic (rovibronic) states $|miJM\rangle$. The rovibronic state is expressed as a product of a vibronic state and rotational state Y_{JM}. Here, J and M are the rotational and magnetic quantum numbers, respectively. The polar axis orientation is along the polarized direction of $\boldsymbol{\mathcal{E}}_{\text{pump}}(t)$. At room temperature, higher-energy rotational states are less populated. Centrifugal distortion effects can be neglected, which ensures the rationality of multiplying a vibronic state with different rotational states Y_{lm}. Inserting $|miJM\rangle$ into Eq. (2) produces vibronic-state QLEs

$$\begin{aligned} i\frac{\partial}{\partial t}\rho_{iJM,jJ'M'}^{mn} = {} & \left(E_{iJ}^m - E_{jJ'}^n\right)\rho_{iJM,jJ'M'}^{mn} \\ & - \mathcal{E}(t)\sum_{o,l,J'',M''}\left(u_{iJM,lJ''M''}^{mo}\rho_{lJ''M'',jJ'M'}^{on}\right. \\ & \left. - \rho_{iJM,lJ''M''}^{mo}u_{lJ''M'',jJ'M'}^{on}\right), \end{aligned} \tag{4}$$

where $u_{iJM,jJ'M'}^{mn} = u_{ij}^{mn}\langle JM|\hat{\mathbf{u}}_{mn}\cdot\hat{\boldsymbol{\mathcal{E}}}|J'M'\rangle$ with $\hat{\mathbf{u}}_{mn}$ and $\hat{\boldsymbol{\mathcal{E}}}$ representing the unit vectors of the TDM element and the electric field. E_{iJ}^m is the eigenenergy of rovibronic state $|miJM\rangle$, which can be expressed as

$$E_{iJ}^m = E_i^m + \left[B_e^m - \alpha_e^m(i+0.5)\right][J+(J+1)]. \tag{5}$$

Here, B_e^m is the rotational constant in the rigid rotor approximation. α_e^m is the rotational-vibrational coupling constant. In Sec. III B, the rotational constants in the example of O_2^+ are taken from NIST [30].

In the above QLEs, we ignore decoherence factors, such as predissociation and spontaneous radiation on typical nanosecond-to-microsecond timescales [31,32] because the maximum delay time is merely 2 ps in our simulations. The QLEs are integrated using the fourth-order Runge-Kutta method with a time step of $\Delta t = 2.5$ a.u. Convergence is tested by reducing the time step in selected calculations. The delay-dependent kinetic energy release (KER) spectrum of fragments in the vibronic-state representation can be expressed as

$$S(E_{\text{KER}}, t_d) = \sum_m \rho_{dis}^{mm}(E_{\text{KER}}, t_d)/p. \tag{6}$$

Here, $E_{\text{KER}}(p) = \frac{1}{2\mu}p^2$ is the kinetic energy with μ and p being the reduced mass and momentum of the fragments, respectively. $\rho_{dis}^{mm}(E_{\text{KER}})$ is the population of the dissociative state with energy E_{KER} on the mth PEC. The QB spectrum in the KER-frequency space is then calculated using

$$P(E_{\text{KER}}, f) = \left|\int dt_d S(E_{\text{KER}}, t_d)e^{-i2\pi f t_d}\right|. \tag{7}$$

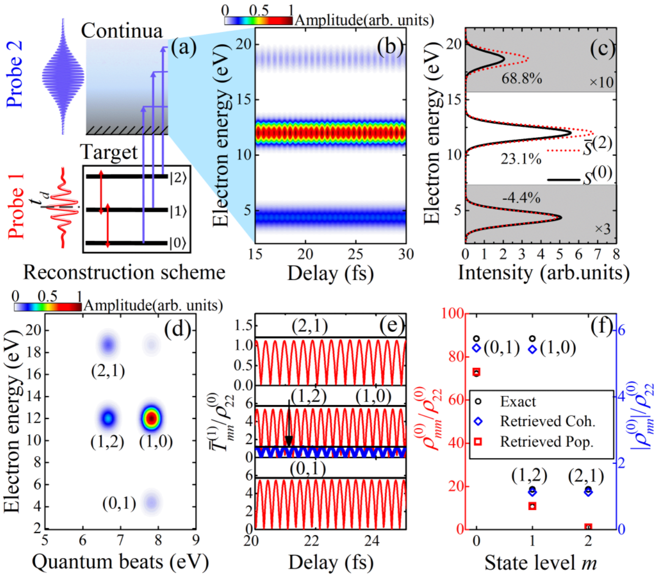

FIG. 1. (a) Illustration of the reconstruction scheme on an one-dimensional H_2^+ model. The potential of H_2^+ is set to be $V(x) = -1/\sqrt{2+(x-1.25)^2} - 1/\sqrt{2+(x+1.25)^2}$ whose eigenenergy of the lowest three bound states are −0.943, −0.656, and −0.410 a.u., respectively. The initial reduced density matrix of the ions is produced via strong-field ionization of H_2 by interacting with a two-cycle 800-nm pulse with an intensity of 1×10^{13} W/cm^2 [33,34]. In the probing step, the target states are coupled by probe 1 (two-cycle, 1×10^{12} W/cm^2 laser pulses with $w_1 = 0.275$ a.u.), then excited to the continua by probe 2 (ten-cycle, 1×10^{13} W/cm^2 laser pulses with $w_2 = 1.1$ a.u.). (b) Delay-dependent photoelectron spectra. (c) Probe-2-only photoelectron spectrum $S^{(0)}$ and delay-averaged photoelectron spectrum $\bar{S}^{(2)}$. For clarity, the first and third peaks are magnified by factors of 3 and 10, respectively. The relative variations are given in percentage form. (d) Quantum beat spectrum of (b). (e) Retrieved time domain signals $\bar{T}^{(1)}_{mn}/\rho^{(0)}_{22}$. Exact $|\rho^{(0)}_{mn}|/\rho^{(0)}_{22}$ are shown as the horizontal lines. (f) Retrieved density matrix elements. The coherences are denoted by (m, n) in the lower panels.

B. Principle of the reconstruction scheme

In this section, we illustrate the reconstruction scheme by taking a three-level H_2^+ model as a prototype whose DM is generated via strong-field ionization of H_2 [33,34]. A sketch of the scheme is presented in Fig. 1(a). Generally, after pump ionization, the ionic system is prepared as a mixed state. The reduced DM is then detected by the delayed probe pulses, which comprise a transition pulse (probe 1) and a narrowband high-frequency excitation pulse (probe 2). These two probes are separated in time and the corresponding electric fields are given by

$$\mathcal{E}_\mathrm{i}(t) = \mathcal{E}_\mathrm{i}^0 e^{-2\ln(2)[(t-t_\mathrm{i}^d)/\tau]^2} \cos\left[\omega_\mathrm{i}\left(t - t_\mathrm{i}^d\right) + \phi_\mathrm{i}\right], \tag{8}$$

where the subscript i = 1, 2 represents probe 1 and probe 2, respectively. Here, τ_i is the pulse duration, $\mathcal{E}_\mathrm{i}^0$ is the electric field amplitude, ω_i is the laser frequency, ϕ_i is the carrier-envelope phase (CEP), which is equal to 0 in calculations, and t_i^d is the center of the probes. In our strategy, the delay time t_d is set as t_1^d. A similar form is used for the pump pulse with the subscript i = pump. The combination of the two probes realizes a two-step process. First, probe 1 couples the target states and mutually transfers their populations. Second, probe 2 excites the target states to their continuous counterparts (photoelectron spectra in the case of the three-state H_2^+ model). The bandwidth of probe 2 must be smaller than the energy gaps among the target states to guarantee state-resolved energy peaks in the continua. Once the TDM elements between the target states and continua are known, population retrieval is intuitive because the intensities of the energy peaks are proportional to the product of the target populations and TDM elements. However, the key problem is that accurate bound-continuum TDM elements are almost impossible to obtain theoretically or experimentally. In the reconstruction scheme, we bypass this difficulty by scrutinizing the relative variations in the peak intensities.

First, we derive the perturbation formula for the DM interacting with the probe-1 pulse. Starting from a pure state $\Phi^{(k)} = \sum_m c_m^{(k)} \psi_m$, where $c_m^{(k)}$ is the amplitude of eigenstate ψ_m, the m-state population at the end of probe 1 t_1^f can be derived based on second-order perturbation theory

$$\begin{aligned} &\left|c_m^{(k)}\left(t = t_1^f; t_d\right)\right|^2 \\ &\quad\approx \left|c_m^{(k,0)}\right|^2 + \sum_n \left|\mathbf{u}_{mn} \cdot \tilde{\boldsymbol{\mathcal{E}}}_1(\omega_{mn})\right|^2 \left(\left|c_n^{(k,0)}\right|^2 - \left|c_m^{(k,0)}\right|^2\right) \\ &\qquad + \sum_n 2\mathrm{Im}\left(\mathbf{u}_{mn} \cdot \tilde{\boldsymbol{\mathcal{E}}}_1^*(\omega_{mn}) c_m^{(k,0)} c_n^{(k,0)*} e^{iw_{mn}t_d}\right). \end{aligned} \tag{9}$$

Here, $c_m^{(k,0)}$ is short for $c_m^{(k)}(t_\mathrm{pump}^f)$, which is the state amplitude at the end of the pump pulse t_pump^f, $\omega_{mn} = E_n - E_m$ is the energy difference, and $\tilde{\mathcal{E}}_1$ denotes the frequency component of probe 1. Then, the population in DM form can be obtained by incoherently superposing $P_k |c_m^{(k)}|^2$ over all k:

$$\begin{aligned} &\rho_{mm}\left(t = t_1^f; t_d\right) \\ &\quad\approx \rho_{mm}^{(0)} + \sum_n \left|\mathbf{u}_{mn} \cdot \tilde{\boldsymbol{\mathcal{E}}}_1(\omega_{mn})\right|^2 \left(\rho_{nn}^{(0)} - \rho_{mm}^{(0)}\right) \\ &\qquad + \sum_n 2\left|\mathbf{u}_{mn} \cdot \tilde{\boldsymbol{\mathcal{E}}}_1(\omega_{mn}) \rho_{mn}^{(0)}\right| \sin\left(\omega_{mn}t_d - \phi_1 + \delta_{mn}^{(0)}\right), \end{aligned} \tag{10}$$

where $\delta_{mn}^{(0)}$ is the phase of $\rho_{mn}^{(0)}$ and $\rho_{mn}^{(0)} = \rho_{mn}(t_\mathrm{pump}^f)$ is the DM element at t_pump^f, which will be reconstructed.

In Eq. (10), the first term is the zero-order term and is the initial m-state population. The second term is a second-order term representing the populations transferred from other target states. The third term represents the interferences between the zero- and first-order perturbation terms, leading to coherent oscillations with different frequencies of ω_{mn}. Clearly, all m-state-related DM elements are encoded in the delay-dependent population $\rho_{mm}(t_d)$. They are then mapped onto the continua via excitations by the probe-2 pulses. From the analysis of energy spectra, the DM can be reconstructed. In the following, we describe our reconstruction strategy in four steps and illustrate each step on the three-state H_2^+ model.

(i) Delay-dependent state-resolved energy spectra $S^{(2)}(E_c, t_d)$ are obtained by performing pump-probe-1-probe-2 operations. Here, E_c denotes the energy of the continuum. The delay-averaged spectrum is then calculated using $\bar{S}^{(2)}(E_c) = \int dt_d S^{(2)}(E_c, t_d)/t_d^{(\mathrm{tot})}$ with $t_d^{(\mathrm{tot})}$ being the total delay time. The maximum intensity at each energy peak is denoted as $\bar{S}_m^{(2)}$, which contains information on the first two terms in Eq. (10). In the case of the three-state model, the delay-dependent photoelectron spectrum is calculated using $S^{(2)}(E_c, t_d) = \sum_m \rho_c^{mm}(p_e^2/2, t_d)/p_e$ with p_e being the electron momentum of the continua. $S^{(2)}$ and $\bar{S}^{(2)}$ are presented in Figs. 1(b) and 1(c), respectively. Detailed laser parameters are given in the Fig. (1) caption.

(ii) The probe-2-only spectra $S^{(0)}(E_c, t_2^d)$ are obtained by performing pump-probe-2 operations. In principle, they are delay independent if the probe-2 bandwidth is sufficiently narrow. The corresponding maximum intensity at each energy peak is denoted as $S_m^{(0)}$, which only contains information on the first term in Eq. (10). In the three-state model, $S^{(0)}$ is depicted as the solid black line in Fig. 1(c).

(iii) When the bound-continuum excitation is a single-photon process, population information is linearly stored in the spectra $\bar{S}^{(2)}$ and $S^{(0)}$. Based on Eq. (10), a set of linear equations relating to the target-state populations can be established at the state-resolved energy peaks

$$\begin{aligned} \frac{\sum_n \alpha_{mn}(\rho_{nn}^{(0)} - \rho_{mm}^{(0)})}{\rho_{mm}^{(0)}} &= \frac{\bar{S}_m^{(2)} - S_m^{(0)}}{S_m^{(0)}} \\ \frac{\sum_n \alpha_{m'n}(\rho_{nn}^{(0)} - \rho_{m'm'}^{(0)})}{\rho_{m'm'}^{(0)}} &= \frac{\bar{S}_{m'}^{(2)} - S_{m'}^{(0)}}{S_{m'}^{(0)}}. \\ \cdots\cdots & \end{aligned} \tag{11}$$

Here, $\alpha_{mn} = |\mathbf{u}_{mn} \cdot \boldsymbol{\mathcal{E}}_1(\omega_{mn})|^2$. With prior knowledge of the TDM $\mathbf{u}_{mn}$ and frequency spectrum $\boldsymbol{\mathcal{E}}_1$ (it can be detected experimentally using a spectrometer), population ratios $\rho_{nn}^{(0)}/\rho_{mm}^{(0)}$ can be retrieved by inverting the above linear equations. In the case of the three-state model, the values of $(\bar{S}_m^{(2)} - S_m^{(0)})/(S_m^{(0)})$ are labeled beside the energy peaks. Using Eq. (11), relative populations are retrieved, which are indicated by red squares in Fig. 1(f). It can be seen that the retrieved values agree well with the exact values (black circles).

(iv) To retrieve coherences, the QB spectrum must be calculated. Figure 1(d) shows the QB spectrum of the delay-dependent signals $S^{(2)}(t_d)$ in the three-state model. Each QB corresponds to one pair of states, labeled as (m, n). By performing the inverse Fourier transform on each isolated QB at its energy peak, oscillation signals $T_{mn}^{(1)}(t_d)$ with a frequency of ω_{mn} can be distilled whose envelope is denoted as $A_{mn}^{(1)}(t_d)$. According to Eq. (10), the relative coherence amplitude can be obtained as

$$\frac{|\rho_{mn}^{(0)}(t_d)|}{\rho_{m'm'}^{(0)}} = \frac{A_{mn}^{(1)}(t_d)}{2\sqrt{\alpha_{mn}} S_m^{(0)}} \frac{\rho_{mm}^{(0)}}{\rho_{m'm'}^{(0)}}. \tag{12}$$

In Fig. 1(e), we display the inverse-Fourier-transformed signals in the form of $\bar{T}_{mn}^{(1)}/\rho_{m'm'}^{(0)} = \frac{|T_{mn}^{(1)}|}{2\sqrt{\alpha_{mn}} S_m^{(0)}} \frac{\rho_{mm}^{(0)}}{\rho_{m'm'}^{(0)}}$. Exact values of $|\rho_{mn}^{(0)}|/\rho_{m'm'}^{(0)}$ are also presented by horizontal lines for comparison. As shown, the amplitudes of the retrieved oscillation signals are slightly smaller than the exact values. These inaccuracies are caused by the high-order perturbation terms and can be reduced by using weaker probe-1 pulses. The retrieved coherence amplitudes are represented as blue diamonds in Fig. 1(f). Furthermore, the phase $\delta_{mn}^{(0)}$ of the coherence $\rho_{mn}^{(0)}$ can be derived directly from the phase at the frequency center of the QB. Note that phase retrieval is not a focus of this study and is not discussed in detail in this paper.

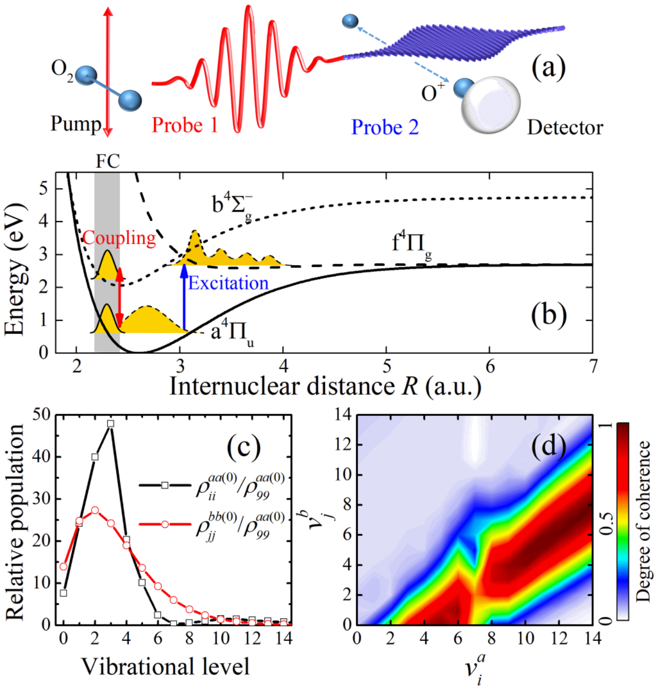

FIG. 2. (a) Illustration of the reconstruction on the O_2^+ system at $\theta = 90^\circ$. The neutral O_2 is first ionized by the pump pulse. Then the generated ionic mixed-state interacts with the probe pulses. The polarized directions of probe 1 and probe 2 are perpendicular. Dissociation signals are detected along the polarized direction of probe 2. (b) Potential energy curves of O_2^+. The gray area represents the region of vertical ionization. (c) The populations and (d) degrees of coherences of the vibronic states at $\theta = 90^\circ$ calculated by the transient ionization model. A 790-nm 15-fs pump pulse with the intensity of 1.5×10^{14} W/cm^2 is adopted to ionize the neutral molecules.

As proof of principle, the reconstruction results for the three-state model demonstrate the feasibility of our scheme. To ensure that the scheme operates normally, several criteria need to be pointed out. First, the number of equations in Eq. (11) should be greater than or equal to $N-1$, where N is the number of target states. Extra equations further restrict relations among the target states, leading to more reliable results. Second, the laser intensity of probe 1 cannot be significantly high because this method operates in the perturbation region. A rough estimate of the intensity is given by $\alpha_{mn} < 0.05$. Third, significant relative variations $(\bar{S}_m^{(2)} - S_m^{(0)})/S_m^{(0)}$ would be beneficial to experimental measurements. This requires large population differences between target states. Such a condition can be readily satisfied in molecular systems because there are always vibronic states at the edge of the FC region with small populations.

III. RESULTS AND DISCUSSIONS

A. Reconstruction of density matrix on O_2^+ without molecular rotation

In this section, we apply the reconstruction method to a strong-field ionized O_2 system without the RDOF. Figure 2(b) displays the related PECs of O_2^+. The vibronic states of the first and second excited electronic states, $a^4\Pi_u$ and $b^4\Sigma_g^-$, respectively, are chosen to be the reconstruction targets, denoted as $v_{i(j)}^{a(b)}$. For these two states, previously calculated spectroscopies using a multireference configuration interaction (MRCI) method have achieved high accuracies [35]. Additionally, various experiments focusing on dissociative ionization and nuclear dynamics on O_2 and its ions were reported [36–39]. The results can be quantitatively reproduced by considering the bound $a^4\Pi_u$, $b^4\Sigma_g^-$, and dissociative $f^4\Pi_g$ states [38]. In the following reconstructions, the dissociation signals are detected to produce the state-resolved energy spectra. Throughout the simulations, dipole transitions from other electronic states are not included since they fall outside the resonant region because of the laser parameters used here.

1. Vibronic-state transient ionization model

Before the reconstruction, we adopt a transient ionization model to assess the reduced DM of O_2^+ after strong-field ionization. This model was originally applied to atomic xenon, and the results were in good agreement with those calculated using the TDCIS method [16]. Recently, we extended this model to molecular systems and verified its validity on a one-dimensional H_2^+ system [34]. For strong-field ionization with multiple vibronic states involved, the DM at the end of the pump pulse t_{pump}^f can be expressed as

$$\rho_{ij}^{mn}\big(t_{\text{pump}}^f\big) = \int_{-\infty}^{t_{\text{pump}}^f} dt \sqrt{\Gamma_i^m(t)\Gamma_j^n(t)} \\ \times \operatorname{sgn}[\mathcal{E}_{\text{pump}}(t)]^{(2-P_m-P_n)/2} e^{i\omega_{ij}^{mn}(t_{\text{pump}}^f - t)}. \tag{13}$$

Here, $\Gamma_i^m(t)$ represents the transient ionization rate from neutral to the ionic state v_i^m at instant time t and can be modeled by the product of the ionization rate at the neutral equilibrium and the FC factor, $\Gamma_i^m[\mathcal{E}_{\text{pump}}(t)] = \Gamma_m[\mathcal{E}_{\text{pump}}(t)] c_i^{m(\text{FC})2}$. $P_{m(n)}$ describes the inversion symmetry of the ionization orbital, with $1(-1)$ representing the $g(u)$ symmetry. This equation can be interpreted as follows. At each ionization instant, a pure state is populated according to the transient ionization rate before propagating freely. Finally, these pure states are superimposed at t_{pump}^f so that a mixed state is constructed. In fact, after each transient ionization, the wave packets still couple with each other under the influence of the residual pump field [34,38]. To account for the laser coupling effect, we prepare the pure-state DM at t as $\rho_{ij}^{mn(\text{ins})}(t) = \sqrt{\Gamma_i^m \Gamma_j^n} \operatorname{sgn}[\mathcal{E}_{\text{pump}}(t)]^{(2-P_m-P_n)/2}$, then propagate it in the residual pump field by solving the QLEs. At the end of the pump pulse, the mixed-state DM reads $\rho_{ij}^{mn} = \int_{-\infty}^{t_{\text{pump}}^f} dt\, \rho_{ij}^{mn(\text{ins})}(t_{\text{pump}}^f, t)$, where $\rho_{ij}^{mn(\text{ins})}(t_{\text{pump}}^f, t)$ is the pure-state DM at t_{pump}^f propagated from t. A more detailed discussion can be found in Ref. [34].

In the simulations, the ionization rate is calculated by the molecular Ammosov-Delone-Krainov (MO-ADK) theory and denoted as $\Gamma_m^{\text{ADK}}(\theta, t)$, which depends on the angle θ between the laser polarization and molecular axis [40]. Using a pump pulse with an intensity of 1.5×10^{14} W/cm^2, we calculate the reduced DM of O_2^+. Taking the angle of 90° as an example, Figs. 2(c) and 2(d) show the vibronic-state populations and degrees of coherences (DOCs), respectively. The DOC between two vibronic states is given by $g_{ij}^{mn} = |\rho_{ij}^{mn}|/\sqrt{\rho_{ii}^{mm}\rho_{jj}^{nn}}$ whose value varies between 0 and 1. As shown, the local maxima of the DOCs are distributed around $\omega_{ij}^{ab} \approx \omega_{\text{pump}}$. This is because the ionization orbitals, $1\pi_u$ for $a^4\Pi_u$ and $3\sigma_g$ for $b^4\Sigma_g^-$, have opposite parities [16,34]. Moreover, it is clear in Fig. 2(c) that the population differences between $v_0^b - v_6^b$ and $v_6^a - v_{14}^a$ are significantly large, which satisfies the third criterion stated in Sec. II B. In this case, the populations transferred from v_j^b to v_i^a will induce large relative variations in the KER peaks, which facilitates experimental measurements.

2. Reconstruction process and results

Now we reconstruct the DM elements of O_2^+ at $\theta = 90°$. The DM calculated using the transient ionization model is henceforth described as "exact." The sketch of the reconstruction is illustrated in Figs. 2(a) and 2(b). Based on the selection rule, the TDM elements of $a^4\Pi_u$-$b^4\Sigma_g^-$ and $a^4\Pi_u$-$f^4\Pi_g$ are perpendicular and parallel to the molecular axis, respectively. Therefore, the polarized direction of probe 1 is set parallel to the pump pulse (0°) to couple the states $a^4\Pi_u$ and $b^4\Sigma_g^-$. The polarized direction of probe 2 is along the molecular axis ($\theta = 90°$) to initiate excitation from $a^4\Pi_u$ to $f^4\Pi_g$. The dissociation signals are detected along the polarized direction of probe 2. For such a three-state system of O_2^+, Eq. (11) needs to be replaced by

$$\frac{\sum_j \alpha_{ij}^{ab}\big(\rho_{jj}^{bb(0)} - \rho_{ii}^{aa(0)}\big)}{\rho_{ii}^{aa(0)}} = \frac{\bar{S}_i^{a(2)} - S_i^{a(0)}}{S_i^{a(0)}}, \tag{14}$$

where $\alpha_{ij}^{ab} = |\mathbf{u}_{ij}^{ab} \cdot \tilde{\boldsymbol{\mathcal{E}}}_1(\omega_{ij}^{ab})|^2$. $\bar{S}_i^{a(2)}$ and $S_i^{a(0)}$ denote the intensities of the v_i^a-state KER peaks of the spectra $\bar{S}^{(2)}$ and $S^{(0)}$, respectively. Because the dipole transition from $b^4\Sigma_g^-$ to $f^4\Pi_g$ is forbidden, the number of linear equations established from the KER peaks always equals the number of target states v_i^a in one set of pump-probe signals. To retrieve the v_j^b-state populations, it is necessary to establish more equations. For this purpose, we adopt two sets of probe-1 pulses with frequencies of 0.05 and 0.055 a.u. Their pulse durations and intensities are two optical cycles and 1×10^{12} W/cm^2, respectively. Under these laser parameters, $v_0^b - v_6^b$ can be resonantly coupled to $v_6^a - v_{11}^a$. To excite $v_6^a - v_{11}^a$ and produce a state-resolved KER spectrum, a 40-fs 635-nm pulse with an intensity of 2×10^{12} W/cm^2 is adopted as probe 2. Note that this wavelength is not unique and other wavelengths can also be used as long as the target states v_i^a are excited to the continua.

Figure 3(a) shows the delay-dependent KER spectra at $\omega_1 = 0.055$ a.u. The energy peaks are separated owing to the narrow bandwidth of probe 2. For each peak, there are weak ∼30 fs and evident 2–3-fs oscillations along the delay time, which intrinsically stem from the vibrational and vibronic coherences, respectively. Here, the words "vibrational" and "vibronic" denote the vibrational states in the same electronic PEC and different electronic PECs, respectively. By averaging the signals over the delay times, the spectrum $\bar{S}^{(2)}$ is obtained, as indicated by the red dashed line in Fig. 3(b). The spectrum $\bar{S}^{(2)}$ at $\omega_1 = 0.05$ a.u. and the probe-2-only spectrum $S^{(0)}$ are also presented as the blue dotted and black solid lines, respectively. Beside each peak, the relative variations are given in percentage form. Given these values, 12 linear equations are

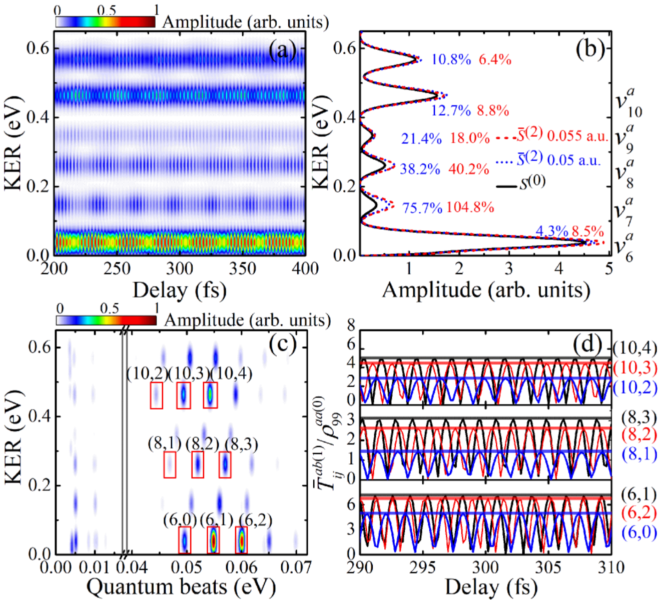

FIG. 3. (a) Delay-dependent KER spectra at $\omega_1 = 0.055$ a.u. (b) Delay-averaged $\bar{S}^{(2)}$ and probe-2-only $S^{(0)}$ spectra. Relative variations $(\bar{S}_i^{a(2)} - S_i^{a(0)})/S_i^{a(0)}$ are given in the form of percentage next to the energy peaks. Corresponding state v_i^a of each peak is labeled on the right. (c) Quantum beat spectrum of (b). (d) The retrieved time-domain signals $\bar{T}_{ij}^{ab(1)}(t_d)/\rho_{99}^{aa(0)}$ from several vibronic QBs [red boxes in (c)]. Exact values of $|\rho_{ij}^{ab(0)}|/\rho_{99}^{aa(0)}$ [labeled by (i, j)] are presented as horizontal lines for comparison. In retrieving the time-domain signals, a Nuttal window is used to improve the signal-to-noise ratio.

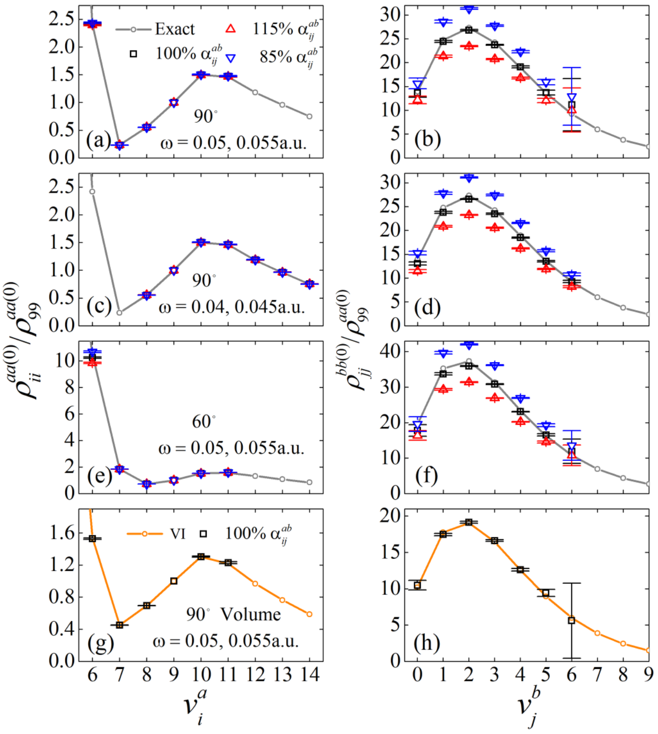

FIG. 4. Retrieved relative populations of (a) v_i^a and (b) v_j^b at $\theta = 90^\circ$ for the case $\omega_1 = 0.05$ and 0.055 a.u. Error bars are given by the standard deviations of the mean values. Results considering the systemic errors of $85\%\alpha_{ij}^{ab}$ and $115\%\alpha_{ij}^{ab}$ are represented as the blue inverted triangles and red triangles, respectively. Exact values are represented as hollow circles connected by solid lines. (c), (d) Same as (a), (b), but with $\omega_1 = 0.04$ and 0.045 a.u. (e), (f) Same as (a), (b), but at $\theta = 60^\circ$. (g), (h) Same as (a), (b), but considering the volume effect. "VI" refers to relative values of the volume-integrated density matrix elements, $\bar{\rho}_{ii}^{aa(0)}/\bar{\rho}_{99}^{aa(0)}$ or $\bar{\rho}_{jj}^{bb(0)}/\bar{\rho}_{99}^{aa(0)}$.

established according to Eq. (14). By inverting the set of linear equations, we retrieve the relative populations of $v_6^a - v_{11}^a$ and $v_0^b - v_6^b$. The results are shown as black squares in Figs. 4(a) and 4(b), where the error bars represent the stability of the reconstruction and will be discussed in the next section. Clearly, the retrieved populations agree well with the exact populations especially for the states $v_6^a - v_{11}^a$.

Next, we reconstruct the coherence amplitudes based on the retrieved relative populations. Figure 3(c) shows the QB spectrum at $\omega_1 = 0.055$ a.u. The vibronic QB reflects the coherence between states v_i^a and v_j^b. Following the reconstruction step (iv), the time-domain signals are obtained by performing the inverse Fourier transform on the QBs at peak crests. Figure 3(d) shows several retrieved signals $\bar{T}_{ij}^{ab(1)}(t_d)/\rho_{99}^{aa(0)}$ whose maximum amplitudes match the exact values $|\rho_{ij}^{ab(0)}|/\rho_{99}^{aa(0)}$ (horizontal lines) well.

So far, our retrieved populations and coherence amplitudes have been in excellent agreement with the exact values for the O_2^+ system. This demonstrates the capability of the scheme in reconstructing the vibronic-state DM for real molecules. Note that the CEPs of the pump and probe-1 pulses must be synchronized when detecting the vibronic coherences to guarantee subcycle time resolution [34]. Otherwise, the vibronic coherences will be hidden in the random fluctuations of the delay-dependent signals, which are usually ignored and regarded as noise signals in experiments. After averaging over delay times, the coherence-induced fluctuations disappear. However, the $\bar{S}^{(2)}$ signals can still be extracted to retrieve the relative populations. In other words, there are no restrictions on the CEPs in the retrieval of populations.

3. Robustness of the reconstruction scheme

In this section, we discuss the robustness and reliability of the reconstruction scheme. From the steps described in Sec. II B, it can be deduced that accurate reconstruction of the DM fundamentally relies on the precise retrieval of the relative populations. According to Eqs. (11) and (14), two types of reconstruction errors will be produced after solving the linear equations. The first is the random error derived from imprecisions in the relative variations $(S_i^{a(2)} - S_i^{a(0)})/S_i^{a(0)}$. These imprecisions can be caused by the experimental measurement errors and the setup instabilities. We simulate the random errors by adding random fluctuations within ±3% to the KER signals at every delay time. By repeatedly performing the reconstruction steps (i) to (iii), a series of retrieved populations are obtained. The resulting random errors are exhibited as error bars on the retrieved values, as shown in Fig. 4. The second type of reconstruction error is referred to as the systematic error. This originates from the inaccurate estimate of α_{ij}^{ab}, which depends on the TDM element u_{ij}^{ab} and the estimate of $\tilde{\mathcal{E}}_1$. Currently, molecular spectroscopic parameters can be calculated via high-level quantum-chemistry-based methods [27,35]. Accuracies in vibronic-state TDM elements are usually verified by comparing the calculated radiative lifetimes with experimental measurements [41,42]. For $\tilde{\mathcal{E}}_1$, the accuracy depends on the calibration of the laser intensity. Generally, traditional calibration methods have large errors when determining laser intensities; for example, when normalizing the signal yields to the ADK rates or calculating the laser intensity at the focus using experimental parameters. However, in recent years, new calibration strategies with a few percent inaccuracies were proposed and achieved [43,44]. Considering the inaccuracy of both u_{ij}^{ab} and $\tilde{\mathcal{E}}_1$, we introduce the systematic error by multiplying α_{ij}^{ab} by a constant of 85% or 115% in Eq. (14). As shown in Figs. 4(a) to 4(f), the systematic errors are exhibited as deviations from the exact values.

For the case of $\omega_1 = 0.055$ and 0.05 a.u., Figs. 4(a) and 4(b) show the retrieved populations with errors. Both the systematic and random errors are larger for states v_j^b than states v_i^a. The reason fundamentally lies in Eq. (14). In effect, it is the relative populations $\rho_{jj}^{bb(0)}/\rho_{ii}^{aa(0)}$ that are being retrieved. Given an inaccuracy of $\rho_{jj}^{bb(0)}/\rho_{ii}^{aa(0)}$, the error of $\rho_{jj}^{bb(0)}$ or $\rho_{ii}^{aa(0)}$ is proportional to its own value. Consequently, the error bars and deviations are larger for states v_i^b with larger populations. For the systematic errors, $85\%\alpha_{ij}^{ab}$ ($115\%\alpha_{ij}^{ab}$) leads to a unified increase (decrease) in the retrieved values. This is because $\rho_{jj}^{bb(0)}/\rho_{ii}^{aa(0)}$ is inversely proportional to α_{ij}^{ab} in Eq. (14). For the random errors, the error bars for v_0^b and v_6^b are especially larger in Fig. 4(b). This is caused by the small values of α_{i0}^{ab} and α_{i6}^{ab}, which connect v_0^b and v_6^b to the KER spectra. Thus, v_0^b and v_6^b can only exert limited influence on the KER spectra. Conversely, slight disturbances in the signals can cause noticeable errors on the retrieved populations of v_0^b and v_6^b.

In our scheme, the target states can be selected by controlling the probe-1 parameters. For example, by changing ω_1 to 0.045 and 0.04 a.u., the states v_i^a with higher energies are resonantly coupled with $v_0^b - v_6^b$. Figures 4(c) and 4(d) show the corresponding retrieved results. As shown, the relative populations of v_8^a-v_{14}^a can be retrieved accurately in this case. To further demonstrate the universality of the scheme, we also proceed with the retrieval at $\theta = 60^\circ$. The results are presented in Figs. 4(e) and 4(f). The different population distributions at $\theta = 60^\circ$ are perfectly recovered. This indicates that tomography of the angular dependent DM can be realized by adjusting the polarized directions of the pump or probe pulses.

Experimentally, depending on where strong-field ionization happens to occur within the pump beam, ionized molecules should be characterized by a position-dependent DM. Actually, with different types of probe-2 pulses, two different levels of reconstructions can be achieved: (1) Reconstruction of the volume-integrated DM and (2) reconstruction of the position-dependent DM. In both cases, the volume effect of the probe-1 pulse can be neglected. This is due to the weak intensity of probe 1, $\sim 10^{12}$ W/cm^2, which is two orders of magnitude lower than that of the pump pulse. Therefore, the probe-1 beam can be loosely focused in the experiment, so that its waist radius is significantly larger than that of the pump beam and the probe-1 spatial intensities are nearly flat within the pump focus. For the reconstruction of the volume-integrated DM, probe 2 is still set to be an IR pulse to induce the one-photon dissociation. Similar to probe 1, the probe-2 pulse is also weak ($\sim 10^{12}$ W/cm^2) and can be loosely focused. Then its waist radius is much larger than that of the pump. The volume effect is only contributed by the pump beam. In the example of O_2^+, the volume-integrated KER spectrum for a pump beam with a spatial peak intensity I_0 is calculated using $S^{(\mathrm{vol})}(I_0) = \int^{I_0} S(I)\frac{\partial V}{\partial I}dI$, where $S(I)$ is the KER signals at a pump intensity I and $\frac{\partial V}{\partial I}dI$ is the differential volume at that intensity [45,46]. Considering a thin ensemble slit along the beam direction, dV can be given in a two-dimensional (2D) configuration $dV = \frac{\pi}{2} l r_0^2 \frac{dI}{I}$ [47]. Here, l and r_0 are the width of the slit and the waist radius of the pump beam, respectively. Using the volume-integrated KER spectra and following the reconstruction steps in Sec. II B, the "effective" DM elements are retrieved. The results are shown in Figs. 4(g) and 4(h). The reconstructed DM elements are compared with the volume-integrated ones, which are expressed as $\bar{\rho}_{ij}^{mn}(I_0) = \int^{I_0} \rho_{ij}^{mn}(I)\frac{\partial V}{\partial I}dI$. Here, $\rho_{ij}^{mn}(I)$ is the intensity (position)-dependent DM. It is clear that the volume-integrated DM elements $\bar{\rho}_{ij}^{mn}$ can still be retrieved quantitatively while considering the volume effect. It is worth noting that $\bar{\rho}_{ij}^{mn}$ is of practical significance. If the volume effect of probe pulses is negligible and the signals are generated via linear processes, such as single-photon dissociation and ionization, the molecule ensemble can be described sufficiently by the volume-integrated DM. To reconstruct the position-dependent DM, broadband extreme ultraviolet or x-ray pulses should be adopted as probe 2 whose beam can be focused to a much smaller size than the pump beam [1,2,48,49]. In this scenario, a well-defined pump-intensity region is selected by probe 2 and the position-dependent DM can be reconstructed by using photoelectron spectra. The procedure is similar to the steps used on the three-state model in Sec. II B, where photoelectron spectra are also used as the continua.

In principle, preparation of the target system is not limited by the ionization mechanisms in the reconstruction of the DM. Whether laser or collision ionization, less-populated vibronic states always exist, which can be used to generate the state-resolved KER spectra. Corresponding KER peaks will possess large relative variations induced by dipole transitions from other target states, which are easier to be measured experimentally and used to reconstruct the DM. However, there is one drawback of using the KER spectra as the energy spectra. Namely, multiple sets of pump-probe experiments must be performed to obtain sufficient equations in such V-type system of O_2^+ ($b^4\Sigma_g^- - a^4\Pi_u - f^4\Pi_g$). This drawback can be overcome by using other state-resolved energy spectra, such as the absorption spectra or the photoelectron spectra. In this case, the relative variations $(S^{(2)} - S^{(0)})/S^{(0)}$ originating from all the target states are simultaneously probed. Sufficient linear equations can be established solely from one set of the pump-probe experiment. The downside is that several of the relative variations would be too small to be detect experimentally. Therefore, high-precision measurement is required. In general, the reconstruction scheme can be readily applied to more complex molecules. The premise is that the target states must be connected by dipole couplings.

B. Reconstruction of density matrix on O_2^+ with molecular rotation

After pump ionization, the ionic DM essentially evolves under the influence of molecular rotation, which has a typical timescale of picoseconds. In this section, we explore the feasibility of the reconstruction while considering molecular rotation.

1. Rovibronic-state transient ionization model

First, we extend the transient ionization model described in Sec. III A to include the RDOF. Generally, for an initial DM, before interaction with any laser pulse, it is assumed that the ensemble of rovibronic states reaches thermal equilibrium [50,51]. In the example of O_2, the rovibronic states in the ground electronic state $X^3\Sigma_g^-$ of O_2 are assumed to be prepared initially in an incoherent manner and populated according to the Boltzmann distribution. At room temperature of $T = 300\ K$, the excited vibrational states of $X^3\Sigma_g^-$ have negligible population, so the rovibronic state can be simply denoted as $|0JM\rangle$, where $|0\rangle$ represents the ground vibrational state of $X^3\Sigma_g^-$. For transient ionization from one single state $|0JM\rangle$ at an instant time t, the released electrons related to different ionic rovibronic states $|miJ^+M^+\rangle$ eventually possess the same momentum at the end of the pump pulse t^f_{pump}. By tracing out the degree of freedom of the free electrons, a coherent superposition of $|miJ^+M^+\rangle$ is established. In the assumption of sudden ionization, the amplitude of $|miJ^+M^+\rangle$ is given by the product of the overlap integral $\langle miJ^+M^+|0JM\rangle$ and the ionization rate $\sqrt{\Gamma_m^{\text{ADK}}(\theta, t)}$. In this case, two conditions guarantee a nonzero amplitude: The first is $M^+ = M$ and the second is that the two rotational states have the same parity. By incoherently summing up the pure states generated from all the rotational states $|0JM\rangle$, a mixed state is produced at t. The corresponding instant DM is given by

$$\rho^{mn(\text{ins})}_{iJ^+M^+,jJ^{+'}M^{+'}}(t) = \langle mi|0\rangle\langle 0|nj\rangle \sum_{J,M} C_J^{\text{Bol}}\langle J^+M^+|\sqrt{\Gamma_m^{\text{ADK}}}$$
$$\times |JM\rangle\langle JM|\sqrt{\Gamma_n^{\text{ADK}}}|J^{+'}M^{+'}\rangle$$
$$\times\ \text{sgn}[\mathcal{E}_{\text{pump}}(t)]^{(2-P_m-P_n)/2}, \qquad (15)$$

where $\langle mi|0\rangle = c_i^{m(\text{FC})}$ is the square root of the vibronic-state FC factor, C_J^{Bol} is the coefficient of the Boltzmann distribution, and the final exponential term represents the parity effect of the electronic ionization orbitals. By integrating over the pulse duration, the rovibronic-state DM at t^f_{pump} is obtained

$$\rho^{mn}_{iJ^+M,jJ^{+'}M}\left(t^f_{\text{pump}}\right) = \int_{-\infty}^{t^f_{\text{pump}}} dt\, \rho^{mn(\text{ins})}_{iJ^+M,jJ^{+'}M}(t)\, e^{-i\omega^{mn}_{iJ^+,jJ^{+'}}(t_f-t)}. \qquad (16)$$

Here, $\omega^{mn}_{iJ^+,jJ^{+'}} = E^m_{iJ^+} - E^n_{jJ^{+'}}$ is the energy gap between two rovibronic states. To account for the dipole coupling effect during the pump pulse, the instant DM, $\rho^{mn(\text{ins})}_{iJ^+M,jJ^{+'}M}$, is further propagated in the residual electric field by solving the rovibronic-state QLEs. Thus, the mixed-state DM at t^f_{pump} is given by

$$\rho^{mn}_{iJ^+M,jJ^{+'}M}\left(t^f_{\text{pump}}\right) = \int_{-\infty}^{t^f_{\text{pump}}} dt\, \rho^{mn(\text{ins})}_{iJ^+M,jJ^{+'}M}\left(t^f_{\text{pump}}, t\right), \qquad (17)$$

where the integrand is the DM element at t^f_{pump} propagated from t.

In the following, we focus on the influence of the RDOF on the vibronic-state DM. First, the rovibronic-state reduced DM of O_2^+ is calculated using Eq. (17) with the same pump pulse used in Fig. 2. In the calculation, only the rovibronic states of $a^4\Pi_u$ and $b^4\Sigma_g^-$ are considered when solving the QLEs during the pump pulse. This is because that the rovibronic states of $f^4\Pi_g$ have negligible effect on the generation of the bound-state DM. After calculating $\rho^{mn}_{iJ^+M,jJ^{+'}M}$, the angular dependent vibronic-state DM is produced by summing up all the rotational states

$$\rho^{mn}_{ij}(\theta) = \sum_{J^+J^{+'}M} \rho^{mn}_{iJ^+M,jJ^{+'}M} Y^*_{J^+M}(\theta) Y_{J^{+'}M}(\theta) e^{i\omega^{mn}_{iJ^+,jJ^{+'}} t_d}. \qquad (18)$$

Figures 5(a) and 5(b) display the angular-dependent v_i^a-state populations at t^f_{pump} without and with the RDOF, respectively. In general, similar patterns are displayed in both cases. Only slight differences are observed around $\theta \approx 0^\circ$. Specifically, the populations at $\theta = 0^\circ$ obey and deviate from the FC distribution in Figs. 5(a) and 5(b), respectively. In the case without the RDOF, the FC distribution is caused by the sudden ionization assumption and the disappearance of the $a^4\Pi_u$-$b^4\Sigma_g^-$ dipole transitions at $\theta = 0^\circ$. In the case with the RDOF, the deviations at $\theta = 0^\circ$ are entirely induced by dipole coupling between the rovibronic states of $a^4\Pi_u$ and $b^4\Sigma_g^-$. For other angles, the population distributions are almost the same in these two cases. To illustrate this point, we present the v_i^a-state populations at $\theta = 90^\circ$ as hollow circles in Figs. 5(a) and 5(b) (right y axis); as shown, they are basically identical. To further compare the coherences in the two cases, Figs. 5(c) and 5(d) show the vibronic DOCs at $\theta = 90^\circ$. Note that their patterns are extremely similar. The maximum value in Fig. 5(d) remains close to 1 when considering molecular rotation. This indicates that the RDOF has limited effects on the generation of the vibronic-state reduced DM when strong-field ionization occurs on a timescale of tens of femtoseconds.

However, as the delay time increases, the RDOF begins to influence the vibronic-state DM. Figure 5(e) shows the v_i^a-state populations at $\theta = 90^\circ$ as functions of the delay time. Note that the populations exhibit revival structures at approximately 4 and 8 ps, which correspond to the 1/4 and 1/2 fractional revivals of $a^4\Pi_u$, respectively. The full rotational revival periods $T_{\text{rev}} = h/(2B_e^m)$ are 15.10 ps for $a^4\Pi_u$ and 12.96 ps for $b^4\Sigma_g^-$. Figure 5(f) presents several vibronic and vibrational DOCs at $\theta = 90^\circ$. As shown, both decrease rapidly with increasing delay time. Specifically, the vibrational DOCs [labeled as $(i, i')_{aa}$] decay exponentially within several picoseconds, whereas the vibronic DOCs [labeled as (i, j)] decay significantly faster within one picosecond, and fluctuate with small values (<0.3) in the subsequent free evolutions. Generally, the distinguishing decoherences originate from the destructive interferences of the rotational states,

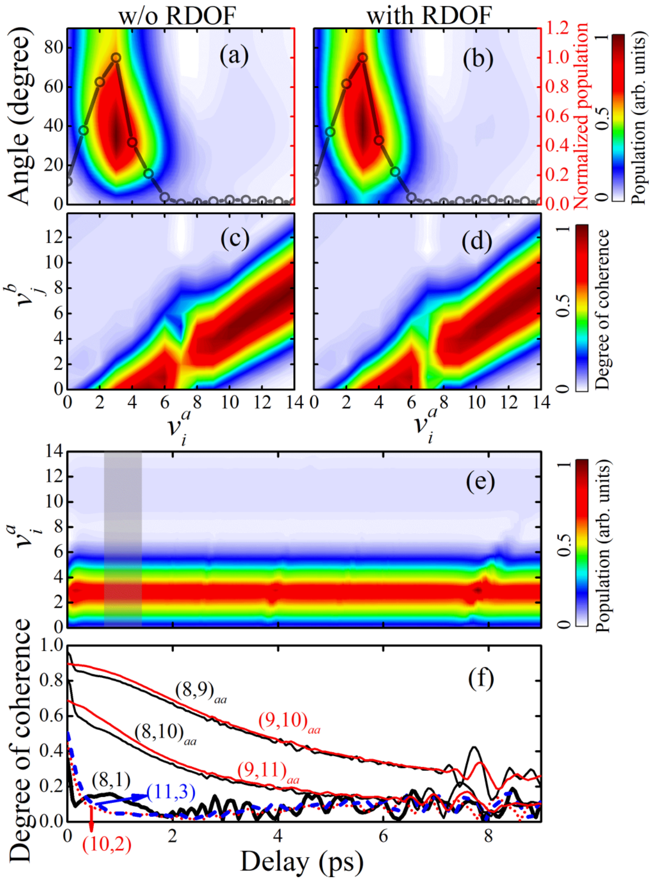

FIG. 5. (a), (b) Angular-dependent v_i^a-state populations (left y axis). The populations at $\theta = 90^\circ$ are depicted as the hollow circles connected by solid lines (right y axis). (c), (d) Degrees of vibronic coherences at $\theta = 90^\circ$. Left panels represent the results calculated by the vibronic-state transient ionization model [without rotational degree of freedom (RDOF)], right panels by the rovibronic-state transient ionization model (with RDOF). (e) v_i^a-state populations at $\theta = 90^\circ$ as functions of the delay time. (f) Several time-evolving vibrational and vibronic degrees of coherences $\theta = 90^\circ$. (i, j) and $(i, i')_{aa}$ represent the vibronic and vibrational state pairs, respectively.

that is, dephasing of the exponential terms in Eq. (18). The energy gaps among the rotational states in the same electronic state are significantly smaller than those in separate electronic states. Therefore, more time is required for the rotational states to become out of phase when they are in the same electronic state, leading to the slower decoherences of the vibrational DOCs.

In terms of electronic coherences, the decoherences and recoherences are found to occur periodically in diatomic molecules owing to nuclear vibrational motions [26,34]. Our theoretical results indicate that, once the RDOF is considered, the electronic recoherences will be attenuated on a timescale as short as subpicosecond because of the rapidly decaying vibronic coherences [see Fig. 5(f)]. This finding agrees with several experimental observations in small molecules, in which the picosecond decays of the electronic coherences produced by either laser excitation or ionization have been probed by high-harmonic or ion spectroscopy [3,52]. For polyatomic molecules, the molecular rotation barely affects the electronic decoherence because coherence typically decays on a timescale of a few femtoseconds. The decoherence mechanism is dominated by the interplay of multiple vibrational modes [18–20].

2. Reconstruction process and results

Essentially, this reconstruction scheme is used to retrieve the DM elements represented by a set of stationary states. Once the RDOF is considered, the vibronic states are no longer stationary, and their populations and coherences evolve over time. However, as shown in Fig. 5(e), the v_i^a-state and v_j^b-state populations are almost constant between adjacent fractional revivals. This feature allows the nearly stable populations to be retrieved using our method. To verify the feasibility, we choose the vibronic-state DM at $\theta = 90^\circ$ as the target. The setups of the pump and probe pulses are the same as in Fig. 2(a). In this case, the magnetic quantum numbers M of $|miJ^+M\rangle$ populated by the pump pulse do not change during the subsequent interactions with the probe-1 pulses. In the calculations, the vibronic-state QLEs [initial DM for each delay is obtained by Eq. (18) with t_d replaced by $t_d - 2.5\tau_1$] and rovibronic-state QLEs provide almost identical population transfers between $a^4\Pi_u$ and $b^4\Sigma_g^-$ when only probe 1 is used. Therefore, as an approximation, we solve the vibronic-state QLEs to calculate the KER spectra in the driving of the two probes. Namely, we assume that the RDOF has limited influence on the results for an interaction with tens-of-femtosecond laser pulses. To further reduce the effects of the RDOF, the probe-2 pulses can be replaced by shorter x-ray pulses generated at the free electron laser (FEL) facility [53].

Subsequently, we apply the reconstruction scheme in the delay interval 700–1400 fs [shaded area in Figs. 5(e) and 6], during which the populations are stable. In the reconstruction, the same probe pulses as in Fig. 4(c) are adopted. Figure 6(a) presents the delay-dependent KER spectra at $\omega_1 = 0.045$ a.u. By comparing this with Fig. 3(a), it is found that the coherent oscillations with the RDOF are much weaker than those without the RDOF. This is considered reasonable since the DOCs significantly reduced after the pump pulse [see Fig. 5(f)]. Following the reconstruction steps (i) to (iii), we retrieve the relative populations, which are shown as hollow squares in the shaded area of Figs. 6(b) and 6(c). The error bars originate from the ±3% random fluctuations of the dissociation signals and are very small so that a stable reconstruction is guaranteed. The populations outside the shaded area are then obtained by calibrating the delay-dependent intensities of the v_i^a-state-resolved KER peaks using solely the probe-2 pulses. These retrieved populations at several delay times are also indicated by hollow squares. Clearly, the retrieved results are in good agreement with the exact values. Based on the retrieved relative populations, the associated vibronic coherences can readily be obtained by performing an inverse Fourier transform on the QBs. Figure 6(d) shows several retrieved time domain signals $\bar{T}_{ij}^{ab(1)}/\rho_{99}^{aa(0)}$. For comparison, the exact values of $|\rho_{ij}^{ab(0)}|/\rho_{99}^{aa(0)}$ are also given as the red dashed lines. The amplitudes of the retrieved signals reproduce the distinguishing decay features of the coherences well.

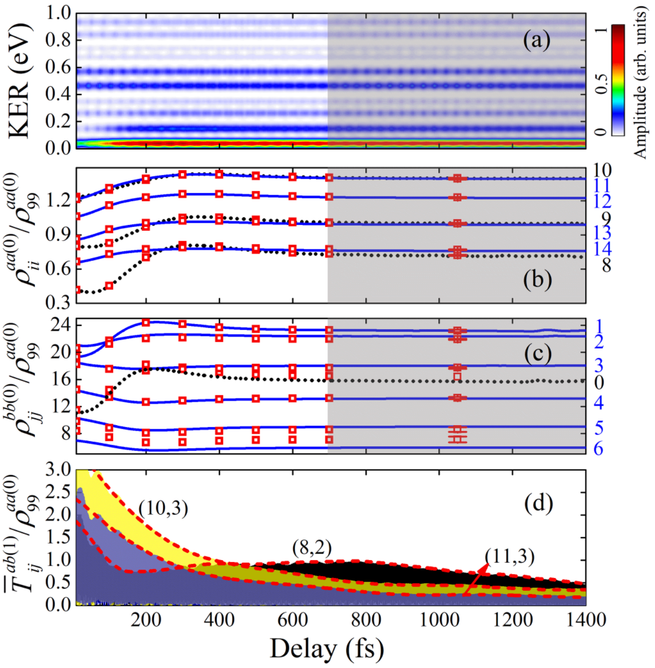

FIG. 6. (a) Delay-dependent KER spectra at $\omega_1 = 0.045$ a.u. Reconstruction strategy is applied in the delay interval 700–1400 fs (shaded area). Retrieved relative populations of (b) v_i^a and (c) v_j^b (hollow squares) at some delay times. Exact populations are shown as the black dotted and blue solid lines. The vibronic states are labeled by i and j at 1400 fs on the right. (d) Several retrieved time domain signals $\bar{T}_{ij}^{ab(1)}/\rho_{99}^{aa(0)}$. Exact relative coherences $|\rho_{ij}^{ab(0)}|/\rho_{99}^{aa(0)}$ [labelled by (i, j)] are shown as the red dashed lines.

This implies that the reconstruction scheme is still capable of retrieving vibronic-state DM elements when considering the RDOF.

In the above reconstructions, the key point is to find a time interval in which the target populations are relatively stable. The stabilities can be verified by analyzing the delay-dependent energy spectra using solely the probe-2 pulses. In the framework of the rovibronic-state transient ionization model, further calculations indicate that population stabilities still exist at higher laser intensities of $\sim 10^{15}$ W/cm^2.

IV. CONCLUSION

In summary, we propose a pump-probe reconstruction scheme to retrieve mixed-state DM elements. This scheme is particularly suitable for the reconstruction of a molecular DM in the basis of vibronic states. We apply the reconstruction scheme to an O_2^+ system produced by strong-field ionization. Quantitative agreements between the retrieved DM elements and the exact values indicate the feasibility of the scheme. Robustness tests indicate that this scheme is reliable against random and systematic errors, which derive from signal instabilities and the inaccurate calibration of laser intensity, respectively. To explore the influence of molecular rotation, we further extend the strong-field transient ionization model by including the RDOF. We find that the RDOF plays a negligible role in the generation of the vibronic-state DM by strong-field ionization on a femtosecond timescale. However, during the subsequent free evolution, dephasing of the rotational states results in decays of the vibronic and vibrational coherences on timescales of subpicosecond to several picoseconds. But the vibronic-state populations remain stable between adjacent fractional revivals. Benefiting from the stabilities, the scheme still works and is capable of reconstructing the evolving DM.

Note that it is essential to ensure the CEPs of the pump and probe pulses are synchronized when retrieving the vibronic coherences. Otherwise, the vibronic coherences will be hidden in random fluctuation signals, while the relative populations remain retrievable. Overall, our reconstruction method is general and can be applied to other complex molecules on the condition that the target states are connected by dipole transitions. The target DM is not limited by generation mechanisms, such as laser excitation or ionization and collision ionization. The key point of the reconstruction is to find a delay interval in which the populations are stable.

ACKNOWLEDGMENTS

This work was supported by the National Natural Science Foundation of China (NSFC) (Grants No. 11904146, No. 11874030, No. 12105131, and No. 12064023), the Natural Science Foundation of Gansu Province (Grant No. 20JR5RA209), and the Scientific Research Program of the Higher Education Institutions of Gansu Province of China (Grant No. 2020A-125).

---

[1] E. Goulielmakis, Z.-H. Loh, A. Wirth, R. Santra, N. Rohringer, V. S. Yakovlev, S. Zherebtsov, T. Pfeifer, A. M. Azzeer, M. F. Kling, S. R. Leone, and F. Krausz, Nature (London) **466**, 739 (2010).

[2] A. Wirth, M. T. Hassan, I. Grguraš, J. Gagnon, A. Moulet, T. T. Luu, S. Pabst, R. Santra, Z. A. Alahmed, A. M. Azzeer, V. S. Yakovlev, V. Pervak, F. Krausz, and E. Goulielmakis, Science **334**, 195 (2011).

[3] P. M. Kraus, S. B. Zhang, A. Gijsbertsen, R. R. Lucchese, N. Rohringer, and H. J. Wörner, Phys. Rev. Lett. **111**, 243005 (2013).

[4] F. Calegari, D. Ayuso, A. Trabattoni, L. Belshaw, S. De Camillis, S. Anumula, F. Frassetto, L. Poletto, A. Palacios, P. Decleva, J. B. Greenwood, F. Martín, and M. Nisoli, Science **346**, 336 (2014).

[5] J. Breidbach and L. Cederbaum, J. Chem. Phys. **118**, 3983 (2003).

[6] J. Breidbach and L. S. Cederbaum, Phys. Rev. Lett. **94**, 033901 (2005).

[7] L. Belshaw, F. Calegari, M. J. Duffy, A. Trabattoni, L. Poletto, M. Nisoli, and J. B. Greenwood, J. Phys. Chem. Lett. **3**, 3751 (2012).

[8] H. Hennig, J. Breidbach, and L. S. Cederbaum, J. Phys. Chem. A **109**, 409 (2005).

[9] H. J. Wörner, C. A. Arrell, N. Banerji, A. Cannizzo, M. Chergui, A. K. Das, P. Hamm, U. Keller, P. M. Kraus, E. Liberatore, P. Lopez-Tarifa, M. Lucchini, M. Meuwly, C. Milne, J. E. Moser, U. Rothlisberger, G. Smolentsev, J. Teuscher, J. A. van Bokhoven, and O. Wenger, Struct. Dyn. **4**, 061508 (2017).

[10] N. Rohringer and R. Santra, Phys. Rev. A **79**, 053402 (2009).

[11] L. Greenman, C. P. Koch, and K. B. Whaley, Phys. Rev. A **92**, 013407 (2015).

[12] R. E. Goetz, A. Karamatskou, R. Santra, and C. P. Koch, Phys. Rev. A **93**, 013413 (2016).

[13] M. Mundt and D. J. Tannor, New J. Phys. **11**, 105038 (2009).

[14] A. Castro, J. Werschnik, and E. K. U. Gross, Phys. Rev. Lett. **109**, 153603 (2012).

[15] S. Pabst, L. Greenman, P. J. Ho, D. A. Mazziotti, and R. Santra, Phys. Rev. Lett. **106**, 053003 (2011).

[16] S. Pabst, M. Lein, and H. J. Wörner, Phys. Rev. A **93**, 023412 (2016).

[17] S. Carlström, J. Mauritsson, K. J. Schafer, A. L'Huillier, and M. Gisselbrecht, J. Phys. B: At. Mol. Opt. Phys. **51**, 015201 (2018).

[18] M. Vacher, L. Steinberg, A. J. Jenkins, M. J. Bearpark, and M. A. Robb, Phys. Rev. A **92**, 040502(R) (2015).

[19] C. Arnold, O. Vendrell, and R. Santra, Phys. Rev. A **95**, 033425 (2017).

[20] M. Vacher, M. J. Bearpark, M. A. Robb, and J. P. Malhado, Phys. Rev. Lett. **118**, 083001 (2017).

[21] C. Leichtle, W. P. Schleich, I. S. Averbukh, and M. Shapiro, Phys. Rev. Lett. **80**, 1418 (1998).

[22] C. Liu, Z. Zeng, R. Li, Z. Xu, and M. Nisoli, Phys. Rev. A **90**, 013403 (2014).

[23] J. A. Cina, J. Chem. Phys. **113**, 9488 (2000).

[24] J. Yuen-Zhou, J. J. Krich, M. Mohseni, and A. Aspuru-Guzik, Proc. Natl. Acad. Sci. **108**, 17615 (2011).

[25] Y. Zhang, T.-M. Yan, and Y. H. Jiang, Phys. Rev. Lett. **121**, 113201 (2018).

[26] Y. Kobayashi, D. M. Neumark, and S. R. Leone, Phys. Rev. A **102**, 051102(R) (2020).

[27] M. Magrakvelidze, C. M. Aikens, and U. Thumm, Phys. Rev. A **86**, 023402 (2012).

[28] L. Cattaneo, J. Vos, R. Y. Bello, A. Palacios, S. Heuser, L. Pedrelli, M. Lucchini, C. Cirelli, F. Martín, and U. Keller, Nat. Phys. **14**, 733 (2018).

[29] H. Timmers, Z. Li, N. Shivaram, R. Santra, O. Vendrell, and A. Sandhu, Phys. Rev. Lett. **113**, 113003 (2014).

[30] K. Huber and G. Herzberg, NIST Standard Reference Simulation Website, NIST Standard Reference Database Number 69, National Institute of Standards and Technology, Gaithersburg, MD, 20899, http://webbook.nist.gov.

[31] P. Erman and M. Larsson, Phys. Scr. **15**, 335 (1977).

[32] A. Carrington, P. G. Roberts, and P. J. Sarre, Mol. Phys. **35**, 1523 (1978).

[33] S. Xue, H. Du, Y. Xia, and B. Hu, Phys. Rev. A **92**, 013420 (2015).

[34] S. Xue, S. Yue, H. Du, B. Hu, and A.-T. Le, Phys. Rev. A **104**, 013101 (2021).

[35] X. Zhang, D. Shi, J. Sun, and Z. Zhu, Mol. Phys. **109**, 1627 (2011).

[36] S. De, M. Magrakvelidze, I. A. Bocharova, D. Ray, W. Cao, I. Znakovskaya, H. Li, Z. Wang, G. Laurent, U. Thumm, M. F. Kling, I. V. Litvinyuk, I. Ben-Itzhak, and C. L. Cocke, Phys. Rev. A **84**, 043410 (2011).

[37] P. Cörlin, A. Fischer, M. Schönwald, A. Sperl, T. Mizuno, U. Thumm, T. Pfeifer, and R. Moshammer, Phys. Rev. A **91**, 043415 (2015).

[38] S. Xue, H. Du, B. Hu, C. D. Lin, and A.-T. Le, Phys. Rev. A **97**, 043409 (2018).

[39] Y. Malakar, F. Wilhelm, D. Trabert, P. Kanaka Raju, X. Li, W. L. Pearson, W. Cao, B. Kaderiya, I. Ben-Itzhak, and A. Rudenko, Phys. Rev. A **98**, 013418 (2018).

[40] S.-F. Zhao, C. Jin, A.-T. Le, T. F. Jiang, and C. D. Lin, Phys. Rev. A **81**, 033423 (2010).

[41] C. M. Marian, R. Marian, S. D. Peyerimhoff, B. A. Hess, R. J. Buenker, and G. Seger, Mol. Phys. **46**, 779 (1982).

[42] K. Okada and S. Iwata, J. Chem. Phys. **112**, 1804 (2000).

[43] S. Micheau, Z. Chen, A. T. Le, J. Rauschenberger, M. F. Kling, and C. D. Lin, Phys. Rev. Lett. **102**, 073001 (2009).

[44] W. C. Wallace, O. Ghafur, C. Khurmi, S. Sainadh U, J. E. Calvert, D. E. Laban, M. G. Pullen, K. Bartschat, A. N. Grum-Grzhimailo, D. Wells, H. M. Quiney, X. M. Tong, I. V. Litvinyuk, R. T. Sang, and D. Kielpinski, Phys. Rev. Lett. **117**, 053001 (2016).

[45] X.-M. Tong, Z. X. Zhao, and C.-D. Lin, Phys. Rev. A **66**, 033402 (2002).

[46] P. Wang, A. M. Sayler, K. D. Carnes, B. D. Esry, and I. Ben-Itzhak, Opt. Lett. **30**, 664 (2005).

[47] J. Posthumus, *Molecules and Clusters in Intense Laser Fields* (Cambridge University Press, Cambridge, England, 2001).

[48] Z.-H. Loh, M. Khalil, R. E. Correa, R. Santra, C. Buth, and S. R. Leone, Phys. Rev. Lett. **98**, 143601 (2007).

[49] S. H. Southworth, D. A. Arms, E. M. Dufresne, R. W. Dunford, D. L. Ederer, C. Höhr, E. P. Kanter, B. Krässig, E. C. Landahl, E. R. Peterson, J. Rudati, R. Santra, D. A. Walko, and L. Young, Phys. Rev. A **76**, 043421 (2007).

[50] B. Friedrich and D. Herschbach, Phys. Rev. Lett. **74**, 4623 (1995).

[51] R. Velotta, N. Hay, M. B. Mason, M. Castillejo, and J. P. Marangos, Phys. Rev. Lett. **87**, 183901 (2001).

[52] A. Rudenko, V. Makhija, A. Vajdi, T. Ergler, M. Schürholz, R. K. Kushawaha, J. Ullrich, R. Moshammer, and V. Kumarappan, Faraday Discuss. **194**, 463 (2016).

[53] J. Ullrich, A. Rudenko, and R. Moshammer, Annu. Rev. Phys. Chem. **63**, 635 (2012).